

## Angular Power Spectra of the *COBE* DIRBE Maps

Edward L. Wright

UCLA Dept. of Physics & Astronomy

### ABSTRACT

The angular power spectra of the infrared maps obtained by the DIRBE (Diffuse InfraRed Background Experiment) instrument on the *COBE*<sup>1</sup> satellite have been obtained by two methods: the Hauser-Peebles method previously applied to the DMR maps, and by Fourier transforming portions of the all-sky maps projected onto a plane. The two methods give consistent results, and the power spectrum of the high-latitude dust emission is  $C_\ell \propto \ell^{-3}$  in the range  $2 < \ell < 300$ .

*Subject headings:* ISM: structure; dust; cosmic microwave background

### 1. Introduction

The angular power spectrum of the sky brightness at millimeter wavelengths can be used to determine the parameters of cosmological models, such as  $H_0$ ,  $\Omega_o$ ,  $\Omega_B$  and  $\Lambda$  (Jungman *et al.* 1996), but our ability to measure this power spectrum will depend on the angular power spectrum of foreground emission from the Milky Way. Kogut *et al.* (1996) have found that free-free emission, which will be the dominant foreground contamination, is better correlated with far infrared dust emission than with synchrotron emission. The angular power spectrum of the dust emission also determines the beam size dependence of the confusion limit to the sensitivity of point source surveys. Gautier *et al.* (1992) found a power spectrum  $P(k) \propto k^{-3}$  for the IRAS 100  $\mu\text{m}$  maps, in a range of  $k$  corresponding to  $200 < \ell < 3000$ , and Kogut *et al.* (1996) found  $C_\ell \propto \ell^{-3}$  for the DIRBE (Boggess *et al.* 1992) 240  $\mu\text{m}$  map in the  $2 < \ell \leq 30$ . But the DIRBE instrument has an angular resolution of  $0.7^\circ$ , which allows one to measure the power spectrum to angular frequencies much higher than  $\ell = 30$ , and DIRBE has 10 bands (240, 140, 100, 60, 25, 12, 5, 3.5, 2.2 and 1.6  $\mu\text{m}$ ) which allow one to measure the frequency dependence of the angular power spectrum. In this note I use a simple method to allow for the effect of detector noise, which dominates the

---

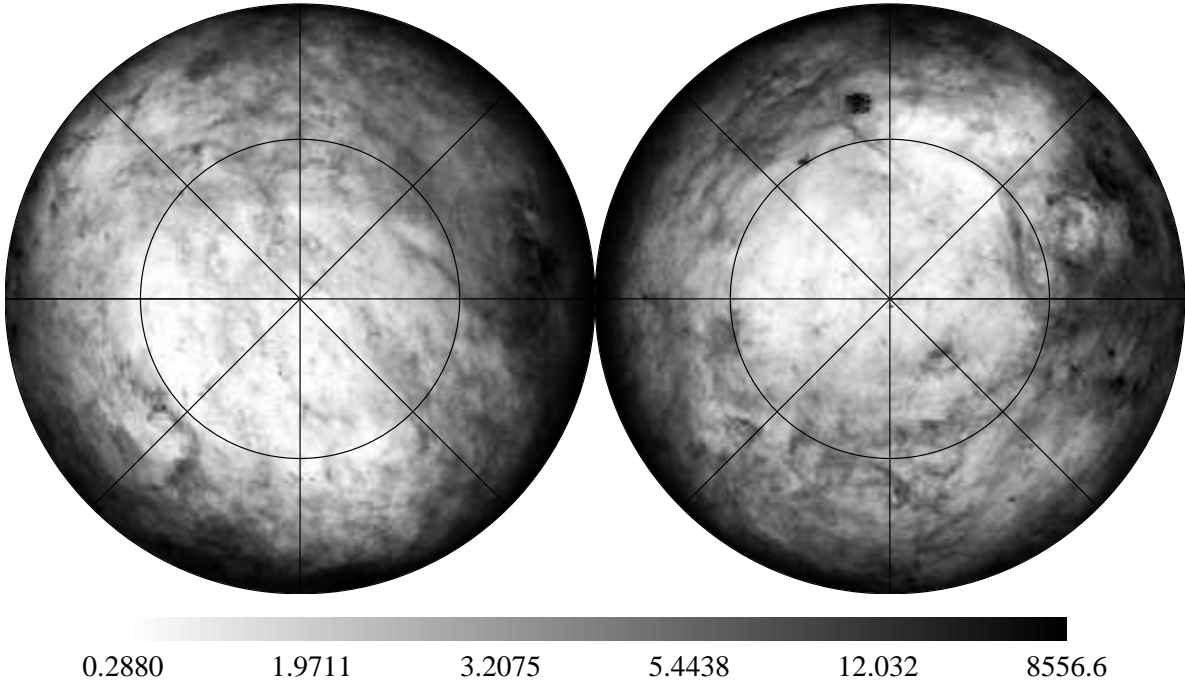
<sup>1</sup>The National Aeronautics and Space Administration/Goddard Space Flight Center (NASA/GSFC) is responsible for the design, development, and operation of the Cosmic Background Explorer (*COBE*). Scientific guidance is provided by the *COBE* Science Working Group. GSFC is also responsible for the development of the analysis software and for the production of the mission data sets.

$100 < \ell$  portion of the DIRBE  $240 \mu\text{m}$  power spectrum, and show that the  $60\text{--}240 \mu\text{m}$  DIRBE maps follow a  $C_\ell \propto \ell^{-3}$  spectrum over the range  $2 < \ell < 300$ . Since this spectrum is more than a full power of  $\ell$  steeper than the predicted spectrum of the cosmic microwave background in inflationary dark-matter dominated models, observations of the “Doppler” peak at  $\ell \approx 200$  should be much less affected by Galaxy than the *COBE* DMR maps.

## 2. Method

The power spectrum of a process is a quadratic function of the data, so noise will bias the power spectrum even if it is not correlated with the signals. The technique used by Wright *et al.* (1994) to correct for this effect in the *COBE* DMR maps was to use the two sides of the DMR instrument, the *A* and *B* sides, to make sum and difference maps,  $S = (A + B)/2$  and  $D = (A - B)/2$ . The noise power spectrum canceled out when the difference in the power spectra of the *S* and *D* maps was taken to yield the the power spectrum of the sky. The DIRBE experiment does not have a comparable duplication of detectors, but I have computed maps with independent detector noises by forming sums of the even weeks and the odd weeks of the data. The DIRBE data have been averaged into separate files for each of the 41 weeks of data taking to allow for the removal of the time varying emission from interplanetary dust. This time variation is due to the motion of the Earth around the Sun, which means that a given spot on the sky is viewed through different parts of the interplanetary dust cloud, and the time variation is used to determine the properties of the interplanetary dust. Once the zodiacal light is removed (see Appendix A), the weeks are summed into all-sky, all-data maps. By summing the even and odd weeks, I make *E* and *O* maps, and construct the sum and difference maps as  $S = (E + O)/2$  and  $D = (E - O)/2$ . Figure 1 shows the sum and difference maps for  $100 \mu\text{m}$  DIRBE maps, while Figure 2 shows the  $240 \mu\text{m}$  maps. The pass 2B DIRBE weekly maps, available since 1994 on the NSSDC, have been used in this paper. Figures 1 and 2 have been histogram equalized, so the values on the scale bar correspond to the  $0^{\text{th}}$ ,  $20^{\text{th}}$ ,  $40^{\text{th}}$ ,  $60^{\text{th}}$ ,  $80^{\text{th}}$  and  $100^{\text{th}}$  percentiles of the map. The difference map at  $240 \mu\text{m}$  is clearly noise dominated, with the middle 60% of the histogram spanning  $1.85 \text{ MJy/sr}$ . A Gaussian distribution with a standard deviation of  $1.1 \text{ MJy/sr}$  would have the same middle 60% span, but the actual distribution of values is not Gaussian due to variable coverage and to errors caused by large sky gradients near the galactic plane. This detector noise is a very significant contribution to the power spectrum of the sum map. The difference map at  $100 \mu\text{m}$  is dominated by a systematic error in the zodiacal light removal caused by an inadequate model for the interplanetary dust cloud, but the overall middle 60% span of  $100 \text{ kJy/sr}$  is very small compared to the sum map. The detector noise in the  $100 \mu\text{m}$  channel on DIRBE is 100 times smaller than the detector noise in the  $240 \mu\text{m}$  channel (Boggess *et al.* 1992) but the middle 60% span of the difference map is only 19 times smaller, showing that the  $100 \mu\text{m}$  difference map is not detector noise dominated. Since the zodiacal light model error has a period of two weeks due to the alternating signs given to successive weeks in the difference map, the dominant spherical harmonic in this difference map is  $\ell = 26$ . The sum map will not have this  $\ell = 26$  power because

## BAND 8 Sum



## BAND 8 Difference

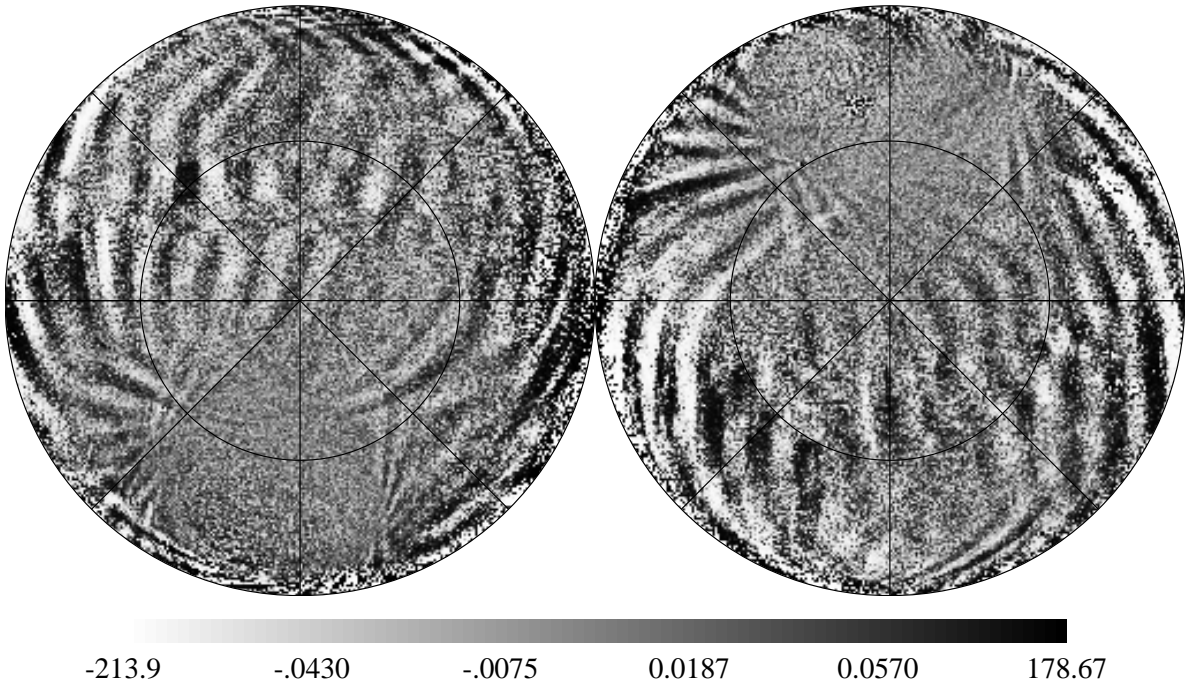
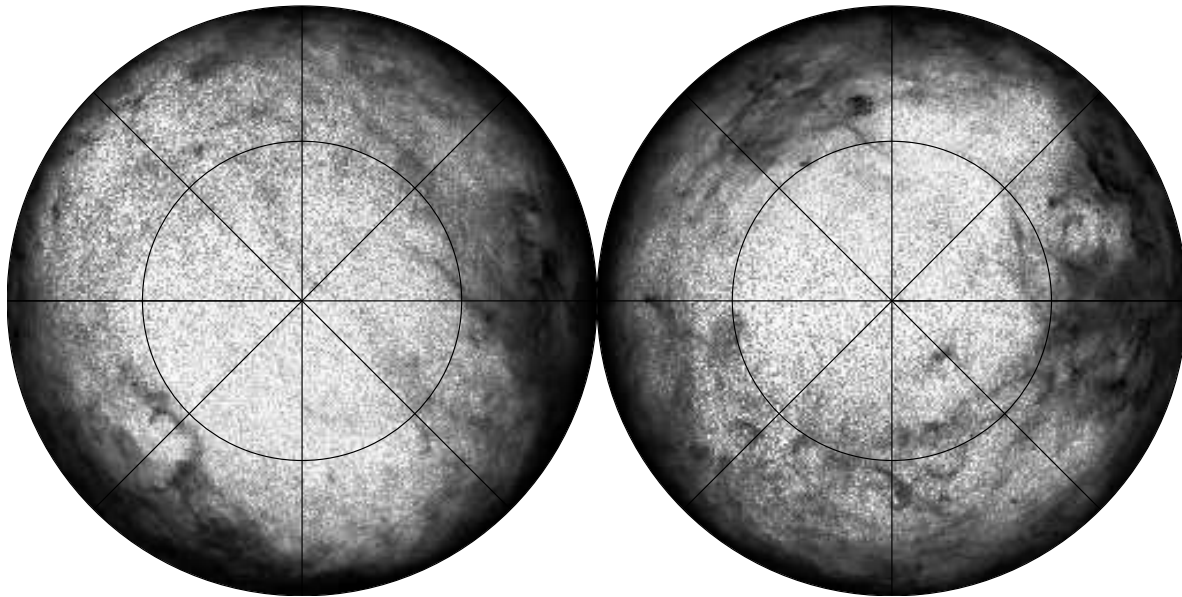


Fig. 1.— Top:  $100\ \mu\text{m}$  map from the sum of the DIRBE even and odd week sum maps. The North Galactic Pole is the center of the left circle, while the South Galactic Pole is the center of the right circle. Bottom: Difference of the even and odd sum maps.

## BAND 10 Sum



## BAND 10 Difference

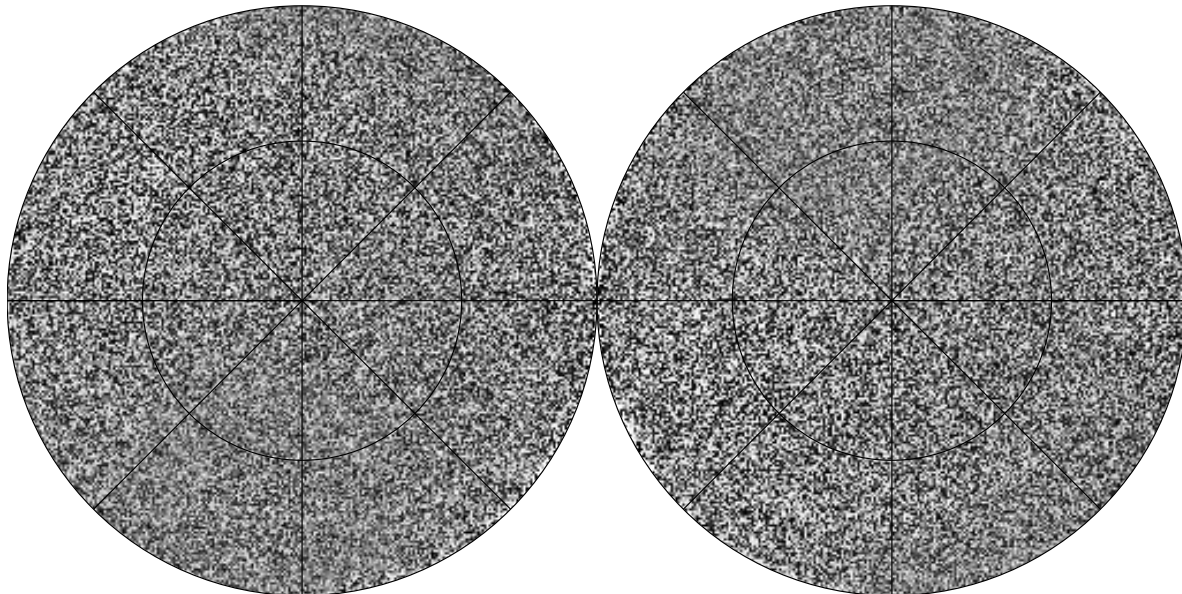


Fig. 2.— Top:  $240\ \mu\text{m}$  map from the sum of the DIRBE even and odd week sum maps. Bottom: Difference of the even and odd sum maps.

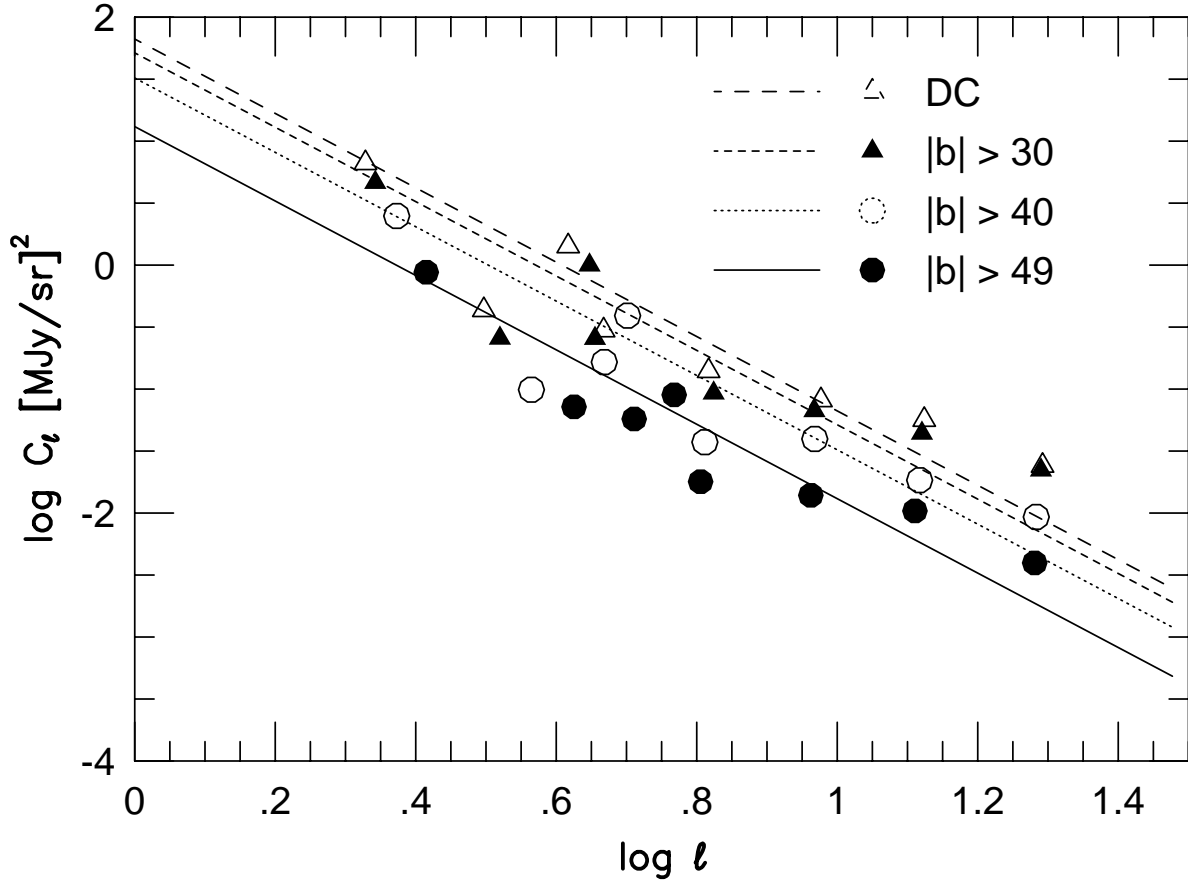


Fig. 3.— Power spectra of the DIRBE 240  $\mu\text{m}$  map after 4 different galactic plane cuts: the “Designer Cut”, and  $|b| > 30^\circ$ ,  $40^\circ$  and  $49^\circ$ . The lines are best fits with an assumed  $\ell^{-3}$  slope.

it does not apply alternating signs to successive weeks, so this method of correcting for noise bias will not work for maps where the zodiacal light errors are comparable to or larger than the true signal. This limits my analysis to the  $\lambda \geq 60 \mu\text{m}$  DIRBE maps. The 25 and 12  $\mu\text{m}$  DIRBE maps are so dominated by the interplanetary dust emission that the residuals due to inadequate models, while only a few percent of the peak emission, are still larger than the high galactic latitude emission from interstellar dust.

### 3. Variation with latitude cutoff

The power spectrum of the DIRBE maps is a strong function of the galactic latitude cutoff. This indicates that the galactic emission is not a stationary Gaussian random process, even after the very bright emission from the Galactic plane has been cut out. Figure 3 shows the Hauser-Peebles (1970) estimate of the power spectrum of the DIRBE 240  $\mu\text{m}$  map with various

cutoff latitudes. The lowest latitude cutoff is labeled DC for “Designer Cut” – this is the same part of the sky used for the analysis of the 4 year DMR maps (Bennett *et al.* 1996). This is basically a  $|b| > 20^\circ$  cut with some further exclusions in Taurus-Orion and Scorpius-Ophiucus, and uses 63% of the sky which is the area given by a straight  $|b| > 22^\circ$  cut. The power spectrum in this “Designer Cut” region is very similar in magnitude to the  $|b| > 30^\circ$  cut, even though the 63% sky coverage of the “Designer Cut” is quite a bit larger than the 50% sky coverage in the  $|b| > 30^\circ$  cut. However, the  $|b| > 40^\circ$  and especially the  $|b| > 48.6^\circ$  cuts give power spectra that are lower still but at a big cost in sky coverage (36% and 25% coverage respectively).

#### 4. High frequency power spectrum

The Wright *et al.* (1994) method of finding power spectra is very slow for large  $\ell$ 's, so an alternative approach using the fast Fourier transform has been used for  $\ell \geq 9$ . The equal area “polar eyeball” projection used in Figures 1 and 2 is used to map one galactic hemisphere onto a square with  $512 \times 512$  pixels. This map is windowed with the function

$$W = \begin{cases} \exp\left(\frac{-(1-\sin|b|)}{1-4(1-\sin|b|)}\right) & \text{for } |\sin b| > 0.75; \\ 0 & \text{otherwise} \end{cases} \quad (1)$$

which vanishes smoothly at  $\sin|b| = 0.75$  or  $|b| = 48.6^\circ$ . Thus only the high latitude 25% of sky is used.

A 2-D fast Fourier transform is then applied to this windowed map. Since the 512 pixel size of the image covered a hemisphere or  $180^\circ$ , the frequency spacing in the output nominally corresponds to  $\Delta\ell = 2$ . However, the use of an equal area projection instead of an azimuthal equidistant projection expands the central portion of the map by a factor  $\pi/\sqrt{8}$ , so the actual output step corresponds to  $\Delta\ell = 2\sqrt{8}/\pi = 1.8$ . The power spectra of the Northern and Southern polar caps were added and then summed into rings of constant  $|k|$ . Finally the power spectrum of the difference map was subtracted from the power spectrum of the sum map to give the power spectrum of the sky. Figure 4 shows the resulting power spectra for DIRBE bands 7-10: 60, 100, 140 and 240  $\mu\text{m}$ . Points with  $\ell \leq 19$  come from the Wright *et al.* (1994) Hauser-Peebles method applied to the sky with  $|b| > 48.6^\circ$ , while the FFT method gives points with  $\ell \geq 9$ . The agreement in the overlap region is good.

#### 5. Comparison with IRAS

The power spectra of several cirrus clouds observed by IRAS are given by Gautier *et al.* (1992) in the form

$$P(\rho) = P(0)(\rho/\rho_0)^\alpha \quad (2)$$

with  $\rho_0 = 0.01$  cycles/arcmin and  $P(0)$  ranging from  $4 \times 10^7$  to  $4 \times 10^{10}$  Jy<sup>2</sup>/sr. In order to convert this to  $C_\ell$ 's I first note that  $\rho_0$  corresponds to  $\ell = 216$  since  $\ell$  is the number of cycles in

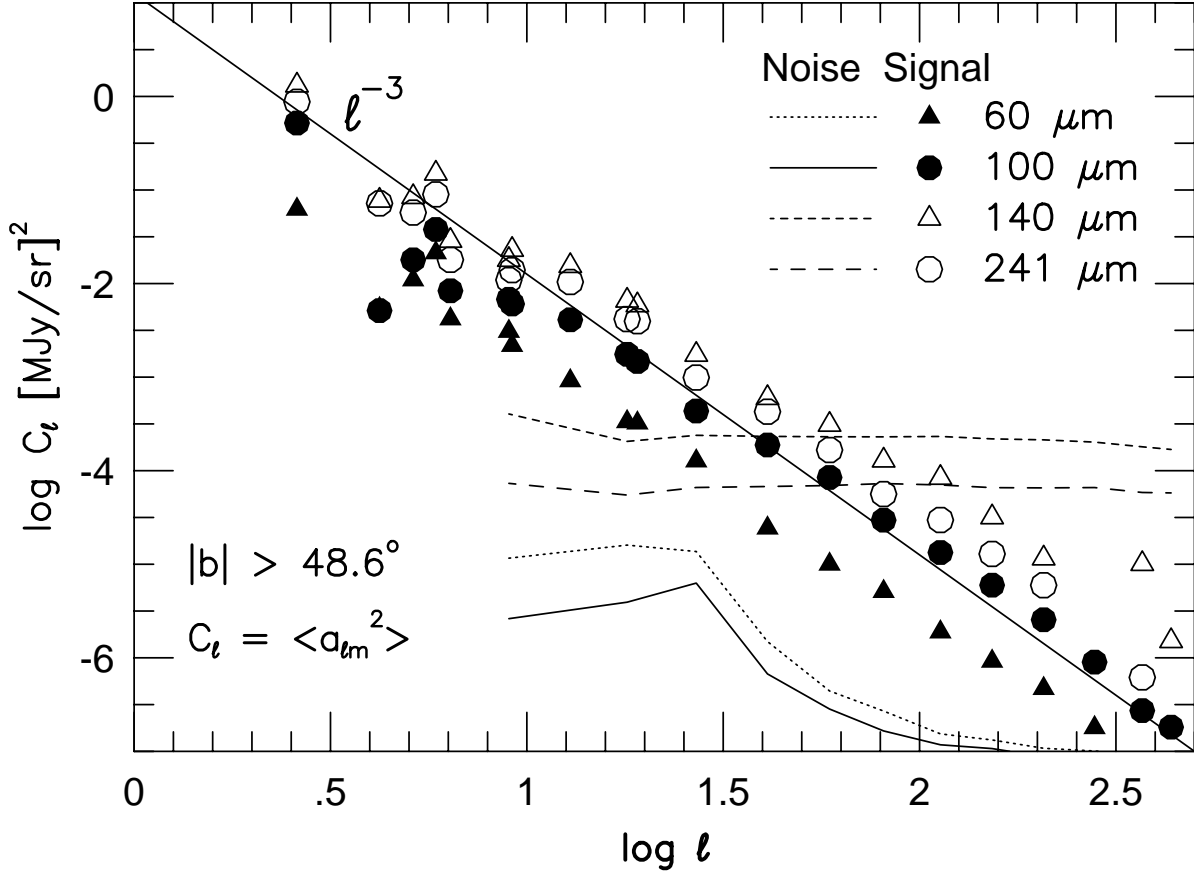


Fig. 4.— Power spectra of the DIRBE 60, 100, 140 and 240  $\mu\text{m}$  maps in  $|b| > 49^\circ$ . The noise spectra for 140 and 240  $\mu\text{m}$  are flat, as expected for a detector noise dominated map. The noise spectra for 60 and 100  $\mu\text{m}$  have a pronounced shoulder at  $\ell = 26$ , which is due to residual zodiacal light modeling error in alternate weeks.

$2\pi$  radians = 21600'. The variance of the sky in a band of frequencies of width  $d\rho = \rho_o$  centered on  $\rho_o$  is  $2\pi\rho_o^2P(0) = 7425 \text{ sr}^{-1}P(0)$ . The same variance computed from  $C_\ell$  is  $(4\pi)^{-1}\ell(2\ell + 1)C_\ell$  at  $\ell = 216$ . These variances are identical so

$$C_\ell = 4\pi^2(\rho/\ell)^2[1 + (2\ell)^{-1}]P(\rho). \quad (3)$$

The factor  $(\rho/\ell)^2 = (4\pi^2\text{sr})^{-1}$  so the net result is that  $C_\ell$  in  $(\text{MJy/sr})^2$  is numerically equal to  $P(\rho)$  in  $\text{MJy}^2/\text{sr}$  except for the negligible  $[1 + (2\ell)^{-1}]$  correction factor.

I estimated the values of  $P(0)$  at  $\rho_o = 0.01$  cycles/arcmin for the power spectra shown in Figure 4 using  $P(0) = \text{median}\{(\ell/216)^3C_\ell\}$ . The values obtained are  $P(0) = 2.2 \times 10^5$ ,  $1.0 \times 10^6$ ,  $3.6 \times 10^6$ , and  $2.1 \times 10^6 \text{ Jy}^2/\text{sr}$  at 60,100, 140, and 240  $\mu\text{m}$ . The value at 100  $\mu\text{m}$  is considerably below the range seen by Gautier *et al.* (1992) in cirrus clouds, but it is higher than their extrapolation to dim cirrus. Since most of the sky with  $|b| > 48.6^\circ$  is quite dim, the IRAS and DIRBE power

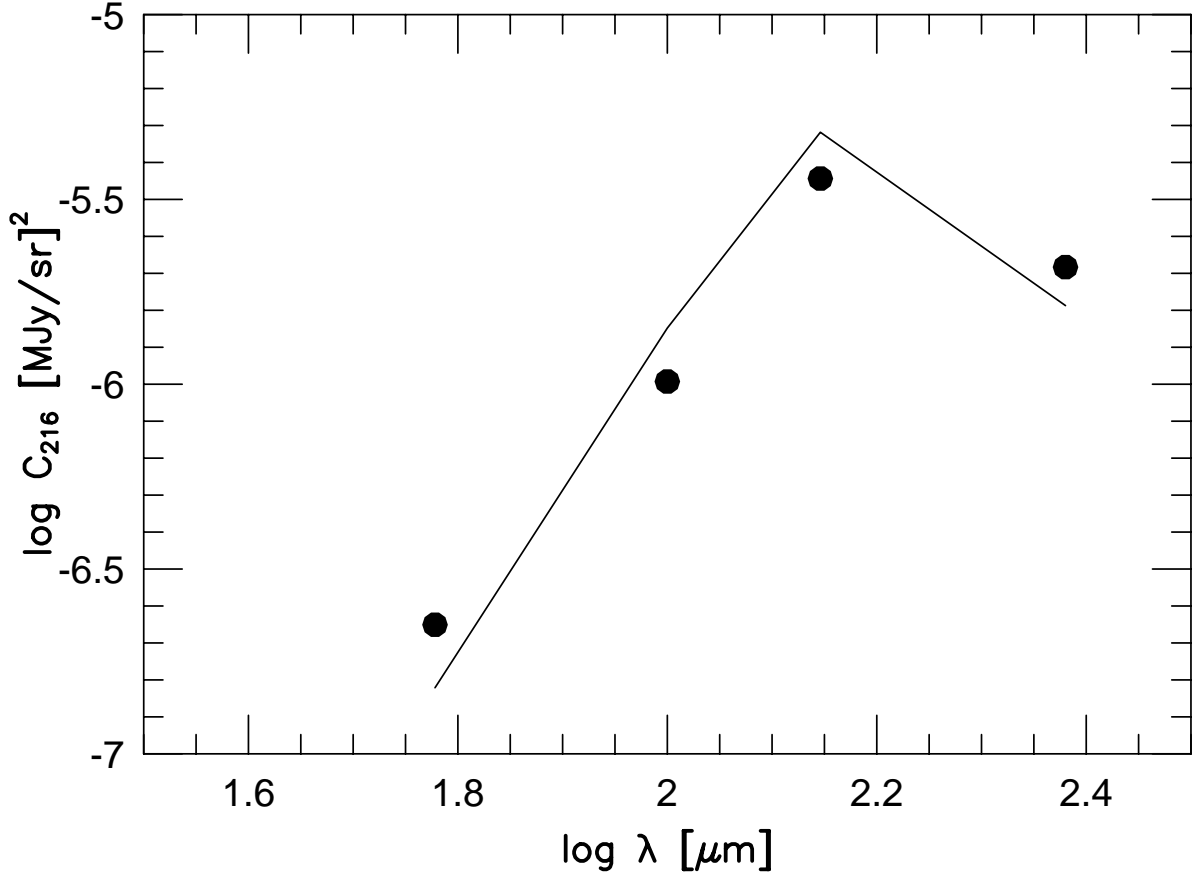


Fig. 5.— Power spectrum amplitude  $C_{216}$  vs. wavelength (points) compared to the square of the galactic flux.

spectra agree reasonably well, with the DIRBE measurement for  $|b| > 48.6^\circ$  only  $2.5\times$  the Gautier *et al.* (1992) estimate for  $|b| > 50^\circ$ .

If the cirrus clouds have the same geometry at all wavelengths, then the power spectrum should scale with frequency like  $C_{216} \propto P(0) \propto F_\nu^2$  where  $F_\nu$  is the flux of a typical cloud. Using the flux of the Milky Way for  $F_\nu$ , I find that

$$C_{216} = P(0) = 10^{-9.74} F_\nu^2. \quad (4)$$

This scaling is shown in Figure 5.

The observed power spectrum can be used to estimate the typical cirrus contribution to the noise using the tables in Gautier *et al.* (1992). With an aperture of  $1.2\lambda/D$ , and subtracting two reference apertures each two aperture diameters away, the expected cirrus noise at  $100 \mu\text{m}$  is  $0.23 \text{ mJy}$  for *SIRTF* and  $0.54 \text{ mJy}$  for *ISO*. These estimates are  $40\%$  smaller than the estimates in Gautier *et al.* (1992). My calculation requires a large extrapolation in angular scale from the  $0.7^\circ$  DIRBE beam to the  $0.5'$  *SIRTF* beam, but no extrapolation to the typical high latitude sky.

The cirrus noise at  $240 \mu\text{m}$  in a 3 meter submillimeter telescope such the planned *FIRST* mission using the same double subtraction scheme is 0.11 mJy. The Milky Way would give a flux 8 times greater than this cirrus noise at  $z = 0.7$  for  $H_o = 50 \text{ km/sec/Mpc}$  and  $\Omega = 1$ .

## 6. Discussion

The angular power spectra of the high galactic latitude infrared sky observed by DIRBE show the same power law behavior seen in the IRAS maps:  $C_\ell \propto \ell^{-3}$ . This is one power of  $\ell$  steeper than the power spectrum expected for the cosmic microwave background, so the problem of galactic contamination in moderate resolution experiments will be smaller than the galactic contamination in the *COBE* DMR maps. Thus proposed new CMB anisotropy experiments that observe with  $\approx 0.5^\circ$  beams will not be ruined by contamination from galactic dust.

The DIRBE data products are the result of dedicated work by hundreds of scientists and engineers who made the *COBE* project a success. I have had many useful discussions with W. Reach, T. Kelsall, M. Hauser and other DIRBE team members about zodiacal light modeling. However, the particular zodiacal light model used in this paper and especially its errors shown in Figure 1 are entirely my own.

### A. Appendix: Zodiacal Light Modeling

The models used in this paper are examples of physical models that integrate a volume emissivity along the the line of sight specified by unit vector  $\hat{n}$ :

$$I_i(\hat{n}, t) = \int \rho(\vec{r}(s)) \left[ \kappa_i D_i(T(R)) + \sigma_i \Phi(\mu) D_i(T_\odot) R^{-2} \right] ds \quad (\text{A1})$$

where  $R = |\vec{r}|$ ,  $\kappa_i$  is a coefficient giving the efficiency in the  $i^{\text{th}}$  DIRBE band of the interplanetary dust grains for thermal emission, while  $\sigma_i$  gives their scattering efficiency.  $\Phi(\mu)$  is the phase function for scattering in terms of  $\mu$ , the cosine of the scattering angle.  $D_i(T)$  is the integral of the Planck function through the DIRBE filter response functions. The position vector  $\vec{r}$  is given by

$$\vec{r}(s) = \vec{x}_\oplus(t) + \hat{n}s \quad (\text{A2})$$

where  $\vec{x}_\oplus(t)$  is the position of the Earth in its orbit around the Sun. The density  $\rho(\vec{r})$  and temperature  $T(R)$  of the interplanetary dust cloud, and the scattering phase function  $\Phi(\mu)$  are all represented by functions with adjustable parameters  $p_i$  having values listed in Table 1. Scaled values of the grain efficiency factors  $\kappa_i$  and  $\sigma_i$  are listed in Table 2 with scalings given by Equations A17 and A18. The values of all the parameters are determined by assuming that all of the observed time variation in the DIRBE signal for a given pixel  $\hat{n}$  is due to the motion of the Earth around the Sun described in Equation A2.

However, the symmetry axis of the zodiacal cloud is not the ecliptic pole but is both tilted and offset (Dermott *et al.* 1994). The tilt is parameterized by the pole unit vector given by

$$\hat{z}_C = \frac{(p_6, p_7, 10)}{\sqrt{100 + p_6^2 + p_7^2}} \quad (\text{A3})$$

The inclination  $i$  with respect to the cloud is specified by

$$\sin i = \frac{\hat{z}_C \cdot \vec{r}}{R}. \quad (\text{A4})$$

The density contours in the cloud are also not centered on the Sun. An offset radius is defined as

$$R_c = R + \vec{o}_C \cdot \vec{r} \quad (\text{A5})$$

where

$$\vec{o}_C = (p_8/10, p_9/10, 0). \quad (\text{A6})$$

The simplest models for the zodiacal cloud assume

$$\rho(\vec{r}) = \rho_o f(i) R_c^{-p_1} \quad (\text{A7})$$

where  $f(i)$  specifies the heliocentric inclination dependence of a fan shaped cloud and  $p_1$  is the exponent of a power law density dependence. The density scaling  $\rho_o$  is fixed at unity and the overall strength of the zodiacal signal is determined by the  $\kappa_i$ 's and the  $\sigma_i$ 's. The temperature dependence is also given by a power law:

$$T(r) = T_o R^{-p_2} \quad (\text{A8})$$

The temperature was fixed at  $R = 1$  au at 280 K because of a strong degeneracy between the  $\kappa_i$ 's and  $T_o$ . The inclination dependence  $f(i)$  is given by

$$\begin{aligned} f(i) &= \exp(-p_3 \times Z^{p_4}) + p_{15} + p_{16} \times \sin^2 i + p_{17} \times 4 \sin^2 i \exp(-4 \sin^2 i) \\ &+ p_{18} \times 16 \sin^2 i \exp(-16 \sin^2 i) + p_{19} \times 36 \sin^2 i \exp(-36 \sin^2 i) \end{aligned} \quad (\text{A9})$$

where  $Z$  is “rounded” absolute value of  $\sin i$ :

$$Z = \begin{cases} |\sin i| - \frac{1}{2}S & \text{for } |\sin i| > S; \\ \frac{1}{2} \sin^2 i / S & \text{for } |\sin i| \leq S. \end{cases} \quad (\text{A10})$$

The break point is given by  $S = \exp(p_5)$ .

The ring of particles resonantly trapped by gravitational perturbations from the Earth (Dermott *et al.* 1994; Reach *et al.* 1995) is modeled using coordinates in a frame rotating to follow  $L_\oplus$ , the mean orbital longitude of the Earth:

$$\begin{aligned} x_D &= x \cos L_\oplus + y \sin L_\oplus \\ y_D &= y \cos L_\oplus - x \sin L_\oplus \\ z_D &= z \end{aligned} \quad (\text{A11})$$

Parameter	Value	Description
$p_1$	1.2186	radial density exponent
$p_2$	0.4451	radial temperature exponent
$p_3$	3.6122	vertical “scale height”
$p_4$	0.9285	vertical density exponent
$p_5$	-1.4766	$\ln(\sin i)$ at break
$p_6$	0.3705	10× cloud pole $x$ component
$p_7$	-0.0736	10× cloud pole $y$ component
$p_8$	-0.0235	10× cloud offset $x$ component
$p_9$	-0.0081	10× cloud offset $y$ component
$p_{10}$	0.7548	10× density contrast of Dermott ring
$p_{11}$	5.5301	$\ln(T_B)$ , band temperature at $R = 1$
$p_{12}$	0.7727	scale factor for bands
$p_{13}$	0.4284	the “dimple” in Dermott’s ring
$p_{14}$	27.7741	vertical scale for Dermott’s ring
$p_{15}$	-0.0251	spherical term in vertical density
$p_{16}$	0.0249	$\sin^2 i$ term in vertical density
$p_{17}$	-0.0456	additional density at $ \sin i  \approx 0.5$
$p_{18}$	-0.1276	additional density at $ \sin i  \approx 0.25$
$p_{19}$	-0.0103	additional density at $ \sin i  \approx 0.17$
$p_{20}$	-0.3133	phase function linear coefficient
$p_{21}$	0.5749	phase function quadratic coefficient

Table 1: Diffuse Cloud Parameters

Then the following terms are defined:

$$L_D = |\text{atan2}(y_D, x_D) + 0.25| \quad (\text{A12})$$

$$A = \begin{cases} \cos(8\pi L_D/3) & \text{for } L_D < \frac{3}{8}; \\ (\cos(8\pi L_D/3) - 1)/2 & \text{for } \frac{3}{8} < L_D < \frac{3}{4}; \\ 0 & \text{otherwise.} \end{cases} \quad (\text{A13})$$

$$D = \exp \left[ -56.5 \left( \sqrt{x_D^2 + y_D^2} - 1.133 + 0.133 p_{13} \exp(-4L_D^2) \right)^2 - \frac{p_{14} z_D^2}{R^2} \right] \quad (\text{A14})$$

The final form for the density is

$$\rho(\vec{r}) = \frac{R}{R_c} f(i) R_c^{-p_1} \left( 1 + \frac{p_{10} D(1+A)}{10} \right). \quad (\text{A15})$$

The phase function for scattering is given by

$$\Phi(\mu) = \exp(-p_{20}\mu + p_{21}\mu^2). \quad (\text{A16})$$

The values of  $\kappa_i$  and  $\sigma_i$  are also adjustable parameters. Only bands 1–3 ( $J$ ,  $K$  and  $L$ ) have non-zero  $\sigma_i$ 's, with

$$\sigma_i = 1.8 p_{21+i} \times 10^{-13} \quad (\text{A17})$$

and only bands 3–10 have non-zero  $\kappa_i$ 's with

$$\kappa_i = 10^{-7} p_{22+i}. \quad (\text{A18})$$

However, this model does not include the IRAS bands (Low *et al.* 1984) The bands are described by more parametrized functions with parameter values given in Table 3. So the following term is added to the intensity:

$$I_B = p_{12} \int \rho_B(\vec{r}(s)) \left[ \kappa_i D_i(T_B(R)) + \sigma_i \Phi(\mu) D_i(T_\odot) R^{-2} \right] ds \quad (\text{A19})$$

with

$$T_B(R) = \frac{\exp(p_{11})}{\sqrt{R}} \quad (\text{A20})$$

The offset and tilt of the bands are given by

$$\hat{z}_B = \frac{(q_5, q_6, 10)}{\sqrt{100 + q_5^2 + q_6^2}} \quad (\text{A21})$$

where  $q_n$  will denote adjustable parameters in the models. The inclination  $i_B$  with respect to the bands is specified by

$$\sin i_B = \frac{\hat{z}_B \cdot \vec{r}}{R}. \quad (\text{A22})$$

Table 2. Scattering and Emission Efficiencies

Parameter	Value	Description
$p_{22}$	0.6864	$\sigma_1$ scaling
$p_{23}$	0.8362	$\sigma_2$ scaling
$p_{24}$	0.6346	$\sigma_3$ scaling
$p_{25}$	2.2829	$\kappa_3$ scaling
$p_{26}$	1.4175	$\kappa_4$ scaling
$p_{27}$	1.2422	$\kappa_5$ scaling
$p_{28}$	1.2996	$\kappa_6$ scaling
$p_{29}$	0.8788	$\kappa_7$ scaling
$p_{30}$	0.7646	$\kappa_8$ scaling
$p_{31}$	0.8243	$\kappa_9$ scaling
$p_{32}$	0.6254	$\kappa_{10}$ scaling

Table 3. IRAS Band Parameters

Parameter	Value	Description
$q_1$	1.3849	$10 \times (\sin i)_{max}$ for Band 1
$q_2$	0.2743	Band 1 normalization
$q_3$	0.2807	$10 \times (\sin i)_{max}$ for Band 2
$q_4$	0.4407	Band 2 normalization
$q_5$	0.1735	$10 \times$ band pole $x$ component
$q_6$	-0.2088	$10 \times$ band pole $y$ component
$q_7$	-1.5723	$10 \times$ band offset $x$ component
$q_8$	-0.2225	$10 \times$ band offset $y$ component
$R_1$	3.14	Outer radius for Band 1
$R_2$	3.02	Outer radius for Band 2

The density contours in the bands are also not centered on the Sun. The offset radius is defined as

$$R_B = R + \vec{o}_B \cdot \vec{r} \quad (\text{A23})$$

where

$$\vec{o}_B = (q_7/10, q_8/10, 0). \quad (\text{A24})$$

The density in the bands is given by

$$\rho_B = \frac{R}{R_B^2} \sum_{j=1}^2 q_{2j} \left[ \begin{cases} \cosh\left(\frac{1.72|\sin i_B|}{q_{2j-1}}\right) & \text{for } |\sin i_B| < q_{2j-1} \text{ and } R_B < R_j; \\ 0 & \text{otherwise.} \end{cases} \right] \quad (\text{A25})$$

The functional form  $\cosh(1.72x)$  was chosen instead of  $(1 - x^2)^{-1/2}$  to avoid numerical problems when integrating through the cusps. Note that the coefficient is chosen so that  $\int_{-1}^{+1} \cosh(1.72x) dx = \pi = \int_{-1}^{+1} (1 - x^2)^{-1/2} dx$ . The outer radii are taken from Jones & Rowan-Robinson (1993).

The band parameters  $\{q_j\}$  and the diffuse cloud parameters  $\{p_i\}$  are optimized in alternating runs. When optimizing the band parameters a set of normal points emphasizing the ecliptic is used. When optimizing the diffuse cloud parameters a separate set of normal points emphasizing the ecliptic poles is used.

A second model that used a slightly different treatment of the Dermott ring and clump was also tried. An additional parameter  $P_1$  describes the radial extent of the ring:

$$D = \exp \left[ -56.5P_1 \left( \sqrt{x_D^2 + y_D^2} - 1.133 + 0.133p_{13} \exp(-4L_D^2) \right)^2 - \frac{p_{14}z_D^2}{R^2} \right] \quad (\text{A26})$$

A second additional parameter  $P_2$  gives a separate adjustment for the density of the “clump” trailing the Earth. The density of the cloud is given by

$$\rho(\vec{r}) = \frac{R}{R_c} f(i) R_c^{-p_1} \left( 1 + \frac{p_{10}D + P_2DA}{10} \right) \quad (\text{A27})$$

Fitting for these parameters gives  $P_2 > p_{10}$  which implies a negative density in the ring+clump system, which seemed unphysical, so the simpler model described above was developed.

## REFERENCES

- Bennett, C. L., Banday, A. J., Gorski, K. M., Hinshaw, G., Jackson, P. D., Keegstra, P., Kogut, A., Smoot, G. F., Wilkinson, D. T. & Wright, E. L. 1996, ApJ, 464, 1-4.
- Bogges, N. et al. 1992, ApJ, 397, 420-429
- Dermott, S. F., Nicholson, P. D., Burns, J. A. & Houck, J. R. 1984, Nature, 312, 505-509.
- Dermott, S. F., Jayaraman, S., Xu, Y. L., Gustafson, B. A. S. & Liou, J. C. 1994. Nature, 369, 719-723.

- Gautier, N., Boulanger, F., Perault, M & Puget, J. L. 1992, AJ, 103, 1313-1324.
- Hauser, M. G. & Peebles, P. J. E. 1973, ApJ, 185, 757-785
- Jones, M. H. & Rowan-Robinson, M. 1993. MNRAS, 264, 237-247.
- Jungman, G., Kamionkowski, M., Kosowsky, A. & Spergel, D. 1996. Phys. Rev. Lett., 76,1007-1010.
- Kogut, A., Banday, A., Bennett, C., Górski, K. & Reach, W. 1996, ApJ, 460, 1.
- Low, F. J., Young, E., Beintema, D. A., Gautier, T. N., Beichman, C. A., Aumann, H. H., Gillett, F. C., Neugebauer, G., Boggess, N. & Emerson, J. P. 1984, ApJ, 278, L19-L22
- Reach, W. T., Franz, B. A., Weiland, J. L., Hauser, M. G., Kelsall, T. N., Wright, E. L., Rawley, G., Stemwedel, S. W. & Spiesman, W. J. 1995. Nature, 374, 521-523.
- Wright, E. L., Smoot, G., Bennett, C. & Lubin, P. 1994, ApJ, 436 443-451.